

# Microkinetic Modeling of the Oxygen Reduction Reaction at the Pt(111)/Gas Interface

Donato Fantauzzi · Tianwei Zhu ·  
Jonathan E. Mueller · Ivo A. W. Filot ·  
Emiel J. M. Hensen · Timo Jacob

Received: 29 October 2014 / Accepted: 18 November 2014 / Published online: 19 December 2014  
© Springer Science+Business Media New York 2014

**Abstract** A microkinetic model of the oxygen reduction reaction (ORR) on Pt(111) under a gaseous H<sub>2</sub> and O<sub>2</sub> atmosphere is used to predict and explain which compositions of H<sub>2</sub> and O<sub>2</sub> lead to the fastest rate of water formation for temperatures between 600 and 900 K. For a stoichiometric (2:1) mixture of H<sub>2</sub> and O<sub>2</sub> the rate-determining step is found to transition from O<sup>★</sup> hydrogenation to O<sub>2</sub><sup>★</sup> dissociation over this same temperature range. These results are explained in terms of the temperature dependence of the surface coverages of O<sup>★</sup> and H<sup>★</sup> and are shown to be consistent with kinetic models aimed at understanding the ORR under electrochemical conditions.

**Keywords** Oxygen reduction reaction · Pt(111) surface · Microkinetic modeling · Surface chemistry · Heterogeneous catalysis · Kinetic rate modeling

## 1 Introduction

The oxygen reduction reaction (ORR) is of fundamental importance to electrochemistry and is crucial for understanding

such varied phenomena as combustion, corrosion and cell respiration. From a technological point of view it is also of great interest since its applications include uses in energy conversion and storage technologies [1–4]. In recent years its central role in powering polymer-electrolyte (or proton-exchange) membrane fuel cells (PEMFCs) has motivated numerous researchers and research groups to search for better ORR catalysts. Platinum has a privileged position among the most commonly used ORR catalysts, and is often used as a benchmark against which the performance of other catalysts is measured. Furthermore, the ORR on Pt(111) serves as a model system, which has been investigated in detail with the goal of being able to elucidate the behavior of other catalysts by analogy to Pt(111).

The ORR on Pt(111) has been looked at under electrochemical conditions in numerous experimental studies [5–7]; however, less attention has been given to the same reaction under non-electrochemical conditions [8–14]. The reactivity of hydrogen with pre-adsorbed atomic oxygen on Pt(111) was studied in the temperature range of 300–450 K using Auger electron spectroscopy (AES) [8]. The dissociation of hydrogen on the surface to provide adsorbed atomic hydrogen, and the size and shape (*i.e.* the availability) of the pre-adsorbed oxygen islands were found to be the key parameters controlling the reactivity. At lower temperatures (200–300 K) a second study used surface titration measurements to support a reaction model, in which oxygen diffusion gives way to an autocatalytic process as the essential reaction process around 250 K [10]. An autocatalytic process was also identified in a later study employing scanning tunneling microscopy (STM) and high resolution electron energy loss spectroscopy (HREELS), in which the desorption temperature of water was identified as the upper temperature limit at which the autocatalytic process plays a major role [11]. More recently temperature-programmed X-ray photoelectron spectroscopy (XPS) was

---

Donato Fantauzzi and Tianwei Zhu have contributed equally to this work.

---

D. Fantauzzi · T. Zhu · J. E. Mueller · T. Jacob (✉)  
Institut für Elektrochemie, Universität Ulm, Albert-Einstein-  
Allee 47, 89069 Ulm, Germany  
e-mail: timo.jacob@uni-ulm.de

I. A. W. Filot · E. J. M. Hensen  
Department of Chemical Engineering and Chemistry, Schuit  
Institute of Catalysis, Eindhoven University of Technology,  
PO Box 513, 5600 MB Eindhoven, The Netherlands  
e-mail: e.j.m.hensen@tue.nl

used to shed further light onto the nature of the autocatalytic process by connecting it with the stability of hydroxyl intermediates, and relating their lifetime to the overall reaction rate [14].

Density functional theory (DFT) has become an important tool in catalysis and surface science over the past couple decades, as it provides mechanistic details not directly available in experiments [15]. Furthermore, DFT calculations can be used to predict the properties of molecules and materials in the rational design of catalysts [16]. Along these lines, DFT calculations have been utilized to investigate the mechanistic details of the ORR on Pt(111) [17–19]. Three different pathways were distinguished: the O<sub>2</sub> dissociation mechanism, the OOH dissociation mechanism and the H<sub>2</sub>O<sub>2</sub> dissociation mechanism. Hydrogen addition within each of these three mechanistic pathways was also considered within two frameworks: Langmuir–Hinshelwood (LH-type) reactions, in which adsorbed hydrogen from the surface is added to the O-containing species, and Eley–Rideal (ER-type) reactions, in which the added hydrogen—in the form of a proton—is supplied directly from the electrolytic phase. For each of these pathways the Gibbs free energy of each reaction step and barrier was calculated including contributions for the solvation energy (using a Poisson–Boltzmann continuum model), zero-point-energy corrections (based on normal modes extracted from the Hessian), entropic contributions to the free energy and the electrode potential. A simple kinetic model was used to relate the calculated energetics to experimental results; however, the absence of a sufficiently sophisticated kinetic model severely restricted these comparisons, and effectively sidelined the predictive power of the computational model.

To remedy this difficulty, Eberle and Horstmann recently implemented the reaction mechanisms and corresponding energetics from the above DFT study into a mean-field kinetic model for the ORR on Pt(111) in acidic media [20]. Unlike several previous studies [21–23], which included fitting parameters to empirical data to bring the model into agreement with experimental results, their model is entirely first-principles-based, and allows the exploration of the influence of the cell voltage on the reaction rate and thus on the current density. Based on their mean-field kinetic model, they were able to distinguish between two electrode potential regimes, in which the ORR primarily proceeds by means of two different reaction pathways, as is manifest in the change in the Tafel slope.

In this letter we present a microkinetic modeling study of the ORR reaction on Pt(111) under a gaseous H<sub>2</sub> and O<sub>2</sub> atmosphere. Following a brief description of our model, we illustrate the importance of using Gibbs free energies in the model as opposed to the activation energies obtained directly from DFT calculations. To gain insight into the

role of each mechanistic step in determining the selectivity and overall activity of the ORR on Pt(111), we carefully examine the case of the stoichiometric (2:1) mixture of gaseous H<sub>2</sub> and O<sub>2</sub> as reactants and simulate the reaction kinetics at temperatures ranging from 600 to 900 K to identify the rate-limiting step as a function of temperature, before considering other ratios of H<sub>2</sub>/O<sub>2</sub> and ultimately determining the ratio of H<sub>2</sub> to O<sub>2</sub> that leads to the fastest overall rate of product formation as function of temperature. Before summarizing our findings, we compare them with other kinetics studies.

## 2 Methods

All microkinetic modeling simulations were performed using the MKM/CXX microkinetic modeling software created by the Inorganic Materials Chemistry group at the Eindhoven University of Technology [<http://www.mkmcxx.nl/>], in which the rate constants of the elementary reaction steps are used within mean field differential equations describing the kinetics of each reaction to model the kinetics of the entire reaction network. Recently, Filot *et al.* used this approach to study the kinetics of the Fischer–Tropsch reaction [24]. Our particular model is based on the eleven elementary reactions illustrated in Fig. 1. The activation energies, zero-point-energy (ZPE) corrections and Gibbs free energies are presented in Table 1 and were taken from Refs. [18, 19, 25]. These activation energies were used to compute temperature-dependent reaction rate constants for each reaction within the context of transition state theory. In doing so the frequency factors were assumed to be equal for all reactions. For the unimolecular adsorption of H<sub>2</sub> and O<sub>2</sub> the reaction rate constant is calculated as:

$$k_{\text{ads}}^i = \frac{A_{\text{site}} P_i \sigma_i}{\sqrt{2\pi m_i k_B T}}, \quad (1)$$

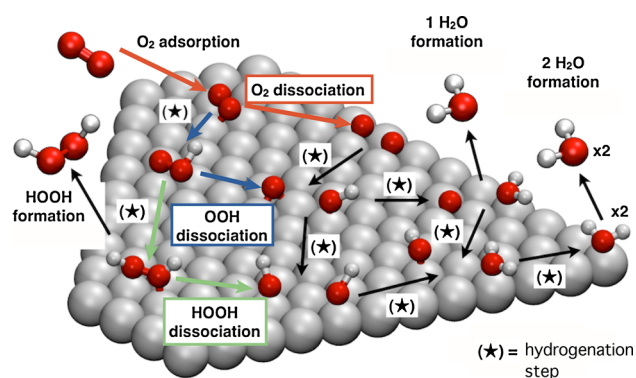


**Fig. 1** Schematic representation of the three investigated ORR mechanisms

**Table 1** Activation energies from Refs. [18, 19, 25] used for calculating reaction rates in the microkinetic model

Elementary reaction step	$\Delta E^\ddagger$ (kJ mol <sup>-1</sup> )	$\Delta E_{\text{ZPE}}^\ddagger$ (kJ mol <sup>-1</sup> )	$\Delta G_{298}^\ddagger$ (kJ mol <sup>-1</sup> )
H <sub>2</sub> O* → H <sub>2</sub> O + *	55 [28]	55 [28]	55 [28]
H <sub>2</sub> O <sub>2</sub> * → H <sub>2</sub> O <sub>2</sub> + *	40	-7	-44
O <sub>2</sub> + * → O <sub>2</sub> *	0	0	0
O <sub>2</sub> * → O <sub>2</sub> + *	15 [27]	15 [27]	15 [27]
H <sub>2</sub> + 2* → 2H*	0	0	0
2H* → H <sub>2</sub> + 2*	72 [26]	72 [26]	72 [26]
O <sub>2</sub> * + * → 2O*	63	61	62
2O* → O <sub>2</sub> * + *	164	164	182
O* + H* → OH* + *	142	142	160
OH* + * → O* + H*	183	167	167
OH* + H* → H <sub>2</sub> O* + *	45	53	75
H <sub>2</sub> O* + * → OH* + H*	124	109	112
O <sub>2</sub> * + H* → OOH* + *	27	36	67
OOH* + * → O <sub>2</sub> * + H*	62	45	62
OOH* + * → O* + OH*	72	65	69
O* + OH* → OOH* + *	178	183	202
OOH* + H* → HOOH* + *	67	78	102
HOOH* + * → OOH* + H*	91	74	74
HOOH* + * → 2OH*	45	34	33
2OH* → HOOH* + *	168	181	202

where  $A_{\text{site}}$  is the area of the adsorption site,  $P_i$  is the partial pressure of component  $i$ ,  $\sigma_i$  is the sticking coefficient of component  $i$ ,  $m_i$  is the mass of component  $i$ ,  $k_B$  is the Boltzmann constant and  $T$  is the temperature. The sticking coefficients of H<sub>2</sub> and O<sub>2</sub> are taken to be unity. In order to account for lateral interactions of adsorbates, adsorption energies obtained from temperature programmed desorption measurements for H<sub>2</sub>, O<sub>2</sub> and H<sub>2</sub>O were employed for the microkinetic simulations [26–28]. The autocatalytic behavior of H<sub>2</sub>O can be ignored because our simulations are being carried out well above its desorption temperature ( $\approx 300$  K). Finally, we only consider the Langmuir–Hinshelwood-type reactions, as these should be most relevant at the Pt(111)/gas interface. The steady-state surface coverages are calculated by solving the differential equations describing the coverage of each of the surface intermediates. These steady-state surface coverages are then used to compute the rates of the individual elementary reaction steps and the overall rate per surface atom. Lateral interactions and their influence on activation barriers are not taken into account in this model.

To help in the identification of the rate-controlling step the degree of rate control,  $X_{\text{RC},i}$ , as defined by:

$$X_{\text{RC},i} = \frac{k_i}{R} \left( \frac{\partial R}{\partial k_i} \right)_{k_j \neq i, K_i} = \left( \frac{\partial \ln R}{\partial \ln k_i} \right)_{k_j \neq i, K_i}, \quad (2)$$

for elementary step  $i$ , where the partial derivative of the overall rate,  $R$ , is taken holding the rate constants ( $k_j$  for all  $j \neq i$ ) for all other steps, and the equilibrium constant  $K_i$  is calculated for each reaction step using the method developed by Campbell [29]. Within transition-state theory, this is accomplished by changing only the free energy for the transition state of step  $i$ , but no other standard-state free energies, reactants, products, or intermediates. The larger the numeric value of  $X_{\text{RC},i}$  is for a given step, the greater its influence on the overall reaction rate  $R$ . A positive value in this sensitivity analysis indicates that increasing  $k_i$  will increase  $R$ . Such steps are termed rate-controlling steps. In contrast, a negative value indicates that an increase in the rate of the step will decrease the overall reaction rate. Such steps are termed inhibition steps.

### 3 Results

To illustrate the sensitivity of the kinetic model to the activation barriers and the importance of including ZPE and thermo-chemical corrections in the calculation of these barriers, we modeled the ORR reaction using only activation energies (red data in Fig. 2), using ZPE-corrected activation energies (green data in Fig. 2), and using enthalpy and entropy corrected activation energies at 298.15 K (*i.e.* Gibbs

free energies corresponding to the blue data in Fig. 2). As can be seen in Fig. 2, there are differences of up to several orders of magnitude in the activity and selectivity of water production in the models, depending on which reaction barriers are used, regardless of temperature. For the remainder of this study we restrict ourselves to models utilizing the Gibbs free energies of activation, because these are the most physically accurate barriers.

Figure 3 presents results for simulations with varying temperatures where the reactant source is a mixture of  $H_2$  and  $O_2$  gases with partial pressures of 2/3 and 1/3 atm respectively. The production of  $H_2O$  is several orders of magnitude higher than the production of  $H_2O_2$  and increases with temperature, as can be seen in rates of reactant production (solid lines in Fig. 3a). Thus, the rates of consumption of  $H_2$  and  $O_2$  (dashed lines) are approximately equal to the whole and the half rate of  $H_2O$  production, respectively. The importance of the various reaction pathways and barriers for the selectivity can be easily seen in the reaction flow diagrams shown in Fig. 4, where the model for 700 K is shown as a representative case (diagrams for other temperatures are available in the Supplementary Material). The major divergence of product to the primary pathway is the strong preference of the  $O_2$ -dissociation and even the  $OOH$ -dissociation pathways over the  $H_2O_2$ -dissociation pathway, since once  $H_2O_2^*$  is formed it is more likely to desorb than to dissociate and continue on the path toward water formation. At low temperature,

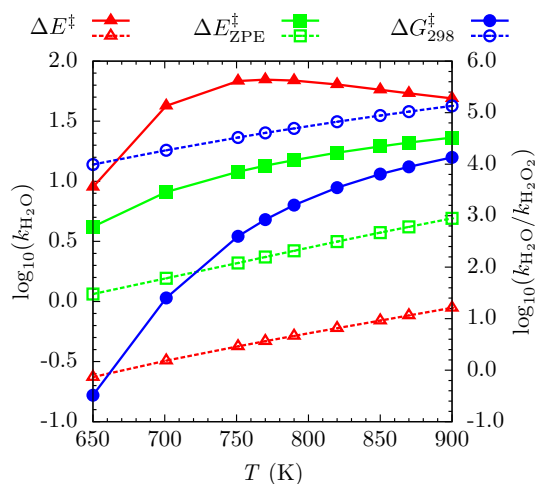


**Fig. 2** Temperature dependence of water formation rates (solid symbols and lines corresponding to  $\log_{10}(k_{H_2O})$ ) and selectivity (hollow symbols and dashed lines corresponding to  $\log_{10}(k_{H_2O}/k_{H_2O_2})$ ) for microkinetic models employing uncorrected activation energies (red symbols and lines corresponding to  $\Delta E^\ddagger$ ), ZPE-corrected activation energies (green symbols and lines corresponding to  $\Delta E_{ZPE}^\ddagger$ ), and room temperature vibrational entropy and enthalpy corrected activation energies (blue symbols and lines corresponding to  $\Delta G_{298}^\ddagger$ )

$O_2^*$  dissociation is inhibited and  $OH^*$  formation is rate-controlling. The reaction order in  $O_2$  is slightly negative as the high coverage of  $O^*$  (see Fig. 3c) prevents  $H_2$  from adsorbing (which is necessary for the oxygen hydrogenation reaction). In accordance, the reaction order in  $H_2$  is positive and the reaction order of  $O_2$  negative (see Fig. 3b). At temperatures above 700 K; the surface starts to expose vacant sites. The  $O_2^*$  dissociation reaction goes from rate-inhibiting to rate-limiting, whereas the oxygen hydrogenation reaction becomes less rate-controlling. At the highest temperatures,  $O_2^*$  dissociation is rate-controlling. The reaction order in  $H_2$  decreases to zero, whereas the order in  $O_2$  increases to 1. The degrees of rate control of these two relevant reaction steps as function of temperature are plotted in Fig. 3d.

In order to better understand the temperature dependence of the degrees of reaction control and rate-controlling step we optimized the reactant composition (*i.e.* the partial pressures of  $H_2$  and  $O_2$ ) for a fixed total pressure of 1 atm at various temperatures. Based on the hypothesis that  $OH^*$  formation needs to be optimized in order to maximize the overall reaction rate, we plotted the product of the surface coverages of  $O^*$  and  $H^*$  (*i.e.*  $[O^*] \cdot [H^*]$ ) as a function of the composition of the reactants. An example of these two plots for 700 K is shown in Fig. 5a, where their correlation is evident. To determine the partial pressure ratios needed to maximize these two quantities (*i.e.*  $k(H_2O)$  and  $[O^*] \cdot [H^*]$ ) we fit a second order polynomial to the five points surrounding the maximum in each curve and found that the ratios of the  $H_2$  and  $O_2$  partial pressures at the two maxima were exactly the same. The importance of maximizing the quantity  $[O^*] \cdot [H^*]$  can help us explain the sensitivity of the overall reaction rate to the dissociation of  $O_2^*$ . Increasing the rate of  $O_2^*$  dissociation would naturally increase the coverage of  $O^*$ , and thus one would expect it to increase the quantity:  $[O^*] \cdot [H^*]$ ; however, at temperatures below  $\approx 780$  K increasing this rate and thus  $[O^*]$  apparently decreases the product:  $[O^*] \cdot [H^*]$ . To understand this we need to take a closer look at what determines the  $H^*$  coverage. The  $H^*$  on the surface is in equilibrium with H-containing species (*e.g.*  $H_2$ ,  $OH^*$ ,  $H_2O^*$ ). In all cases the formation of  $H^*$  requires an empty site, and the consumption of  $H^*$  creates an empty site. Thus the population of  $H^*$  is directly proportional to the population of empty sites,  $[^*]$ . Now by decreasing  $[O^*]$ , we increase  $[^*]$ , which results in an increase in  $[H^*]$ . When the ratio  $[O^*] : [H^*]$  is large, then the product  $[O^*][H^*]$  is more sensitive to changes in  $[H^*]$  than to changes in  $[O^*]$ . This is the case at low temperatures and so we can see why the dissociation of  $O_2^*$  becomes inhibitive as  $O^*$  becomes

**Fig. 3** Results from models with stoichiometric mixtures of H<sub>2</sub> and O<sub>2</sub> reactants, with a total constant pressure of 1 atm: **a** reaction rates of reactant consumption (*hollow symbols and dotted lines*) and product formation (*solid symbols and lines*), **b** reaction order and apparent activation energies, **c** surface coverages of major surface components (all other surface species have negligible coverages), and **d** degree of rate control for critical reaction steps (degree of rate control for all other reaction steps are negligible)

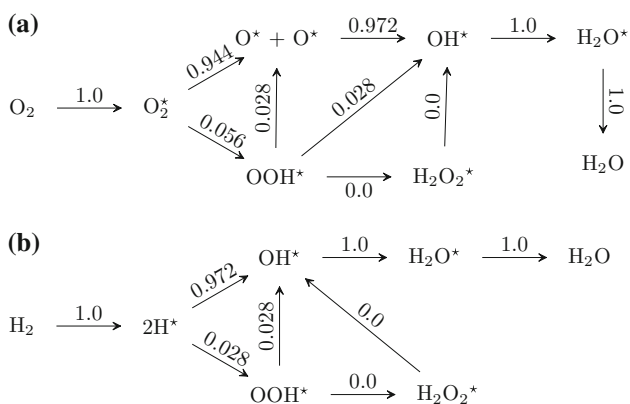
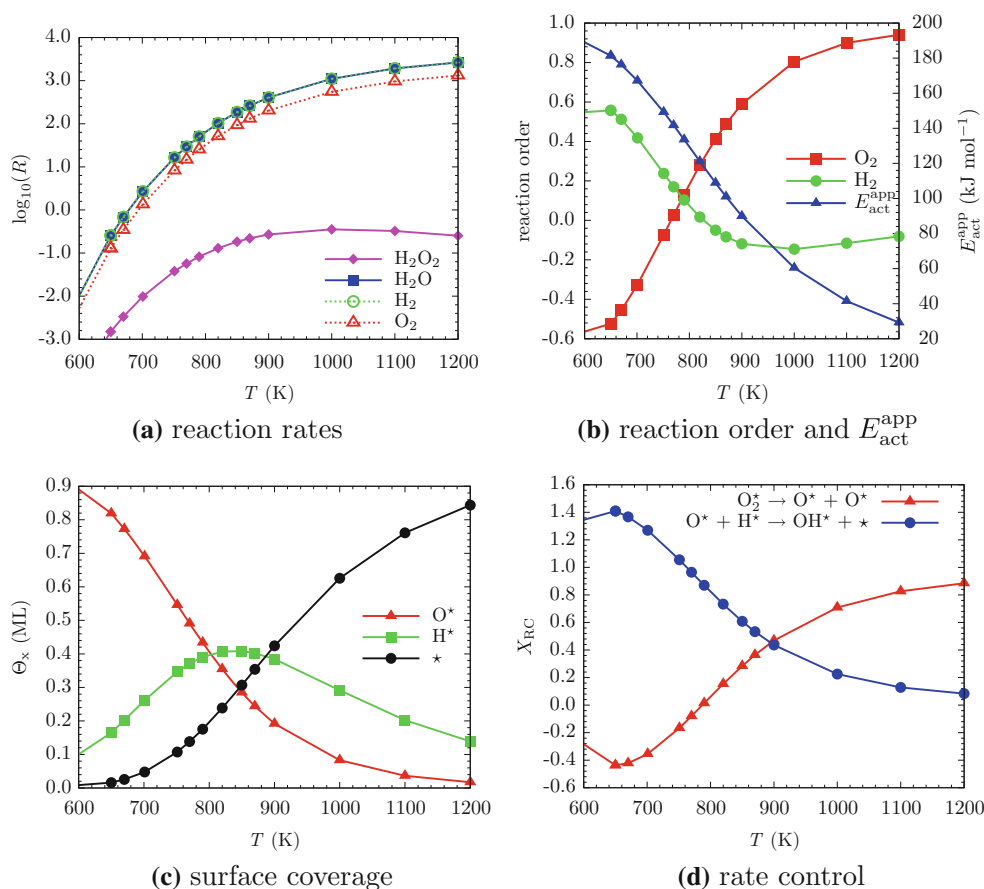


**Fig. 4** Reaction maps showing the flow of **a** O<sub>2</sub> and **b** H<sub>2</sub> through the reaction network at 700 K. Values correspond to fractions of **a** oxygen and **b** hydrogen passing through each reaction. Reaction maps for other temperatures are available in the SM

the major surface species, and begins to effectively block H<sub>2</sub> from dissociating on the surface to form H\*. At higher temperatures [O\*] decreases significantly, effectively removing the capacity it had to inhibit H<sub>2</sub> dissociation by occupying large fractions of the surface.

The reactant mixtures needed to obtain the fastest overall reaction rate from 1 atm of total reactants at temperatures

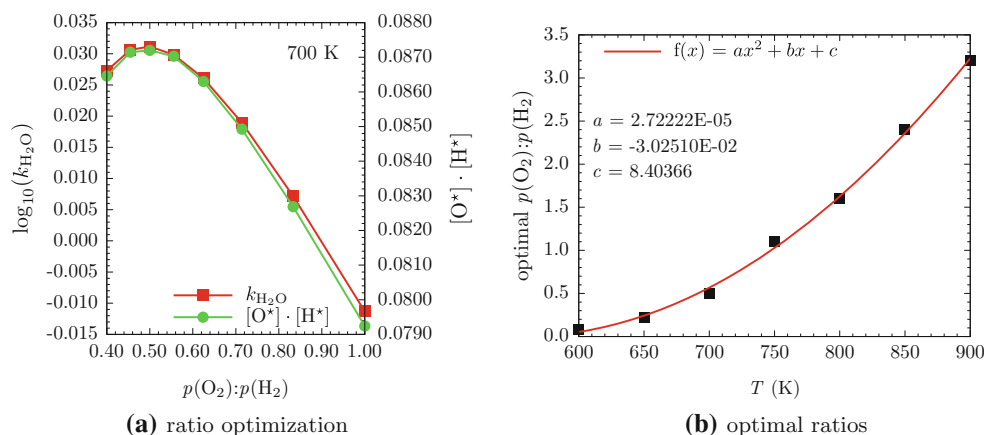
ranging from 600 to 900 K are plotted in Fig. 5b. A second-order polynomial was fit to the data points in order to aid interpolation between the data points and is plotted along with them. The need for larger fractions of H<sub>2</sub> at lower temperatures to drive the reaction is due to the tendency of O\* to occupy a majority (or near majority) of surface sites at low temperatures, and the way this restricts the coverage of H\* as evident in the inhibitive nature of O<sub>2</sub>\* dissociation at low temperatures. At high temperatures the surface is mostly free, and so larger partial pressures of O<sub>2</sub> are needed to drive the dissociation of O<sub>2</sub>\* which has become the rate-controlling step in the formation of H<sub>2</sub>O. The trend from H<sub>2</sub>-rich mixtures driving faster kinetics at lower temperatures to O<sub>2</sub>-rich mixtures doing so at higher temperatures can be seen in Fig. 6, in which the water formation rates for a variety of reactant mixtures (all with a total pressure of 1 atm) are plotted as a function of the temperature.

### 4 Discussion

Comparing our results with those of other kinetic models can only be meaningfully done if we keep in mind critical differences between the models and the diverse reaction



**Fig. 5 a** Plots of product formation rates ( $k_{\text{H}_2\text{O}}$ ) and the product of the coverages of  $[\text{O}^*]$  and  $[\text{H}^*]$  as function of the ratio of the partial pressures of  $\text{H}_2$  and  $\text{O}_2$  visually demonstrating the correspondence of their maxima, **b** ratio of  $\text{O}_2$  to  $\text{H}_2$  partial pressures for a fixed total pressure of 1 atm that maximizes the rate of water production



conditions they were designed to represent. As already mentioned above, so far there are no mikrokinetic models for the catalytic water formation on Pt out of gaseous  $\text{H}_2$  and  $\text{O}_2$ , although this should be the first logical step when investigating the full electrochemical oxygen reduction reaction. Therefore, here we can only compare to available studies of the electrochemical ORR, but should keep in mind the subtle, and not so subtle, differences in the models. The mean-field model used by Eberle and Horstmann to study the ORR in acidic media included the ER-type reactions for the hydrogenation steps [20], which we emitted, as they are unlikely in a gaseous rather than electrolytic environment. Because the barriers for the ER-type reactions are significantly smaller than the equivalent LH-type barriers, the ER pathways were dominant in their model. This stands in stark contrast to the gas-phase system studied here, in which only LH pathways are available. Thus, it is no surprise that we do not observe the change in mechanistic pathway from  $\text{O}_2$  dissociation to OOH and  $\text{H}_2\text{O}_2$  dissociation that they observe, since the low energy ER pathways make the hydration of  $\text{O}_2^*$  a more energetically favorable process than its dissociation. Furthermore, the chemical potentials for O and H in the range of

cell voltages they consider do not necessarily correspond to the chemical potentials in the partial pressures and temperatures used in our models. This likely explains why we find only significant surface coverages of  $\text{O}^*$  and  $\text{H}^*$ , while they find cell voltages with significant surface coverages of not only  $\text{O}^*$  and  $\text{H}^*$ , but also  $\text{OOH}^*$ ,  $\text{O}_2^*$  and  $\text{OH}^*$ . Similar results to those of Eberle and Horstmann were obtained by Jinnouchi et al. using a mean field model also developed for describing the ORR under electrochemical conditions [23]. Indeed, they also noted that the protonation of  $\text{O}^*$  is the rate-controlling step for the ORR in their model under electrochemical conditions, as it is in ours at the Pt(111)/gas interface. However, they found that the OOH-dissociation pathway (they do not consider the  $\text{H}_2\text{O}_2$ -dissociation pathway) is favored over the  $\text{O}_2$ -dissociation pathway for the electrode potentials they considered ( $U > 0.6$  V), in agreement with Eberle and Horstmann for this potential range. Only the  $\text{O}_2$  dissociation pathway was considered by Wang *et al.* in their double-trap kinetic model, which includes only four possible reaction steps, in their efforts to characterize the ORR reaction at the Pt(111)/aqueous electrolyte interface [22]. Thus, comparing our gas phase model with these electrochemical models highlights similarities and differences between the ORR carried out in these two very different environments. In both cases the hydrogenation of  $\text{O}^*$  is a rate-controlling step; however, the availability of low barrier ER-type reactions under electrochemical conditions makes the different reaction pathways more competitive with each other and leads to faster overall reaction rates, but lower selectivity.

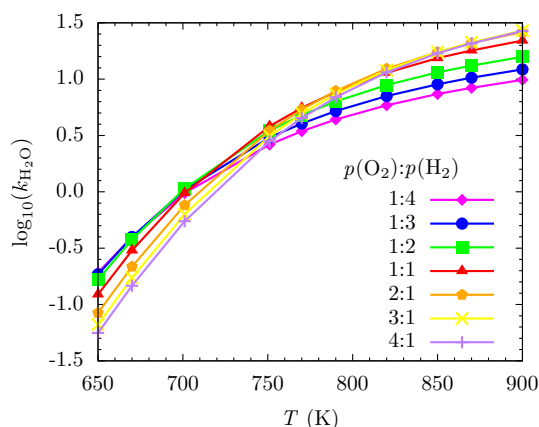


**Fig. 6** Reaction rates for water formation for various mixtures of  $\text{O}_2$  and  $\text{H}_2$  (with a total pressure of 1 atm) as a function of temperature

## 5 Summary

In summary, we have presented a mikrokinetic model of the ORR reaction on Pt(111) under a  $\text{H}_2$  and  $\text{O}_2$  gas atmosphere with a total pressure of 1 atm. We have demonstrated the sensitivity of the model to the activation

barriers and thereby stressed the crucial importance of using Gibbs free energies in kinetic models as opposed to the activation energies obtained directly from DFT calculations. For a stoichiometric (2:1) mixture of H<sub>2</sub> and O<sub>2</sub> as the source of reactants we found that the rate-determining step changes from OH\* formation from O\* to O<sub>2</sub>\* dissociation as the temperature increases from 600 to 900 K. By noting that the product of the O\* and H\* coverages correlates with the overall reaction rate and that the fraction of unoccupied surface sites increases with temperature, we are able to explain why the dissociation of O<sub>2</sub>\* is the rate-controlling step at high temperatures, but becomes inhibiting below 780 K. Finally, we computed the partial pressures of H<sub>2</sub> and O<sub>2</sub> (out of a total pressure of 1 atm) at which our model predicts the fastest rate of water formation as a function of temperature. Therefore, the present work paves the way for future microkinetic modeling studies of the electrochemical oxygen reduction reaction.

## References

1. Adžić R (1998) *Electrocatalysis*. Wiley, New York, pp 197–242
2. Marković NM, Ross PN Jr (1999) *Interfacial electrochemistry: theory, experiments and applications*. Marcel Dekker, New York
3. Marković NM, Schmidt TJ, Stamenković V, Ross PN (2001) *Fuel cells* 1(2):105
4. Ross PN (2003) *Handbook of fuel cells: fundamentals, technology, applications*. Wiley, New York
5. El Kadiri F, Faure R, Durand R (1991) *J Electroanal Chem Interfacial Electrochem* 301(12):177
6. Marković NM, Adžić RR, Cahan BD, Yeager EB (1994) *J Electroanal Chem* 377(12):249
7. Marković NM, Gasteiger HA, Ross PN (1995) *J Phys Chem* 99(11):3411
8. Gland JL, Fisher GB, Kollin EB (1982) *J Catal* 77(1):263
9. Mitchell GE, Akhter S, White JM (1986) *Surf Sci* 166(23):283
10. Verheij LK, Freitag M, Hugenschmidt MB, Kempf I, Poelsema B, Comsa G (1992) *Surf Sci* 272(13):276
11. Völkening S, Bedürftig K, Jacobi K, Wintterlin J, Ertl G (1999) *Phys RevLett* 83(13):2672
12. Sachs C, Hildebrand M, Völkening S, Wintterlin J, Ertl G (2002) *J Chem Phys* 116(13):5759
13. Qi L, Yu J, Li J (2006) *J Chem Phys* 125(5):054701
14. Näslund LA (2013) *Surf Sci* 618:42
15. Groß A (2002) *Surf Sci* 500:347
16. Besenbacher F, Chorkendorff I, Clausen BS, Hammer B, Molenbroek AM, J.K. Nørskov I (1998) *Stensgaard. Science* 279(5358):1913
17. Jacob T (2006) *Fuel Cells* 6(3–4):159
18. Keith JA, Jacob T (2010) *Angew Chem Int Ed* 49(49):9521
19. Keith JA, Jerkiewicz G, Jacob T (2010) *ChemPhysChem* 11(13):2779
20. Eberle D, Horstmann B (2014) *Electrochim Acta* 137:714
21. Park YK, Aghalayam P, Vlachos DG (1999) *J Phys Chem A* 103(40):8101
22. Wang Y, Balbuena PB (2005) *J Phys Chem B* 109(31):14896
23. Jinnouchi R, Kodama K, Hatanaka T, Morimoto Y (2011) *Phys Chem Chem Phys* 13(47):21070
24. Filot IAW, vanSanten RA, Hensen EJM (2014) *Angew Chem Int Ed* 53(47):12746
25. Mueller JE, Fantauzzi D, Jacob T (2013) *Multiscale Model Electrochem Syst*. Wiley, New York
26. Miller JT, Meyers BL, Modica FS, Lane GS, Vaarkamp M, Koningsberger DC (1993) *J Catal* 143(2):395
27. Gland JL (1980) *Surf Sci* 93(23):487
28. Grecea ML, Backus EHG, Riedmiller B, Eichler A, Kleyn AW, Bonn M (2004) *J Phys Chem B* 108(33):12575
29. Campbell CT (2001) *J Catal* 204(2):520